Monthly Notices of the ROYAL ASTRONOMICAL SOCIETY

MNRAS **506,** 4993–5004 (2021) https://doi.org/10.1093/mnras/stab2051
Advance Access publication 2021 July 19

Flux conservation, radial scalings, Mach numbers, and critical distances in the solar wind: magnetohydrodynamics and *Ulysses* observations

Daniel Verscharen [1,2]★ Stuart D. Bale[3,4,5,6] and Marco Velli[7]

[1]*Mullard Space Science Laboratory, University College London, Holmbury House, Dorking RH5 6NT, UK*
[2]*Space Science Center, University of New Hampshire, Durham, NH 03824, USA*
[3]*Physics Department, University of California, Berkeley, CA 94720-7300, USA*
[4]*Space Sciences Laboratory, University of California, Berkeley, CA 94720-7450, USA*
[5]*The Blackett Laboratory, Imperial College London, London SW7 2AZ, UK*
[6]*School of Physics and Astronomy, Queen Mary University of London, London E1 4NS, UK*
[7]*Department of Earth, Planetary, and Space Sciences, University of California Los Angeles, Los Angeles, CA 90095, USA*

Accepted 2021 July 13. Received 2021 July 7; in original form 2021 April 18

ABSTRACT

One of the key challenges in solar and heliospheric physics is to understand the acceleration of the solar wind. As a super-sonic, super-Alfvénic plasma flow, the solar wind carries mass, momentum, energy, and angular momentum from the Sun into interplanetary space. We present a framework based on two-fluid magnetohydrodynamics to estimate the flux of these quantities based on spacecraft data independent of the heliocentric distance of the location of measurement. Applying this method to the *Ulysses* data set allows us to study the dependence of these fluxes on heliolatitude and solar cycle. The use of scaling laws provides us with the heliolatitudinal dependence and the solar-cycle dependence of the scaled Alfvénic and sonic Mach numbers as well as the Alfvén and sonic critical radii. Moreover, we estimate the distance at which the local thermal pressure and the local energy density in the magnetic field balance. These results serve as predictions for observations with *Parker Solar Probe*, which currently explores the very inner heliosphere, and *Solar Orbiter*, which will measure the solar wind outside the plane of the ecliptic in the inner heliosphere during the course of the mission.

Key words: MHD – plasmas – methods: data analysis – Sun: heliosphere – solar wind.

1 INTRODUCTION

The Sun, like most other stars, continuously emits a magnetized plasma in the form of the solar wind (Verscharen, Klein & Maruca 2019). This super-sonic and super-Alfvénic flow fills the interplanetary space and removes mass, momentum, energy, and angular momentum from the Sun. The acceleration mechanisms of the solar wind remain poorly understood and pose one of the greatest science questions in the field of solar and heliospheric physics. Since the early time of the space age, starting in the early 1960s, a fleet of spacecraft have measured the properties of the solar wind at different locations in the heliosphere. The *Ulysses* mission (Wenzel et al. 1992; Balogh 1994; Marsden 2001), in operation from 1990 until 2009, plays a special role amongst them due to its unique orbit that led the spacecraft above the Sun's poles, enabling studies of the solar-wind parameters as functions of heliolatitude. These studies are of great importance to the question of the solar-wind acceleration, since they enable the separation of different solar-wind source regions and their relationships to the heliolatitude-dependent magnetic-field structure in the corona (Neugebauer 1999). Before *Ulysses*, all solar-wind missions were restricted to quasi-equatorial orbits. These measurements could only be used to explore heliomagnetic latitudes up to $\pm 25^\circ$ (Bruno et al. 1986), exploiting the tilt between the Sun's magnetic dipole axis and its rotation axis. The knowledge about the dependence of solar-wind parameters on radial distance and heliolatitude helps constrain models for our understanding of the acceleration of the solar wind. For example, comparisons of *in situ* mass-flux measurements with coronagraph observations suggest that the solar wind requires an additional deposition of energy to the contribution from thermal conduction alone (Munro & Jackson 1977) as assumed in the classic Parker (1958) model of the solar wind. Moreover, measurements of the plasma's mass flux can be linked to photospheric measurements of the magnetic field, which provide us with insight into the location and the magnetic nature of the solar-wind heating processes (Wang 2010). *Ulysses* data confirm this need for additional energy deposition also in polar wind (Barnes, Gazis & Phillips 1995).

Ulysses observations corroborated the bimodal structure of the solar wind during solar minimum (McComas et al. 1998a, b): near the Sun's equator at heliolatitudes below approximately $\pm 20^\circ$, the wind is variable and slow (radial flow speeds $\lesssim 400\,\mathrm{km\,s^{-1}}$); in polar regions, the wind is steadier and fast (radial flow speeds $\gtrsim 700\,\mathrm{km\,s^{-1}}$). During solar maximum, this bimodality vanishes almost completely, and the solar wind exhibits large variations in its plasma and field parameters (McComas et al. 2000). The

★ E-mail: d.verscharen@ucl.ac.uk

measurements have been effectively visualized in polar plots, in which the polar angle indicates the heliolatitude and the distance from the origin indicates the solar-wind parameter (e.g. speed and density, see McComas et al. 2000, Plate 1). These comprehensive studies of *Ulysses* data also provide us with fit results for solar-wind parameters depending on heliocentric distance and heliolatitude (see also Ebert et al. 2009).

Although the Sun's mass and energy loss due to the solar wind are insignificant throughout the Sun's life cycle, the loss of angular momentum carried away by the solar wind is significant for the Sun's long-term evolution. The solar-wind particles begin their journey in the corona in co-rotation with the Sun. At some distance, the particles are released from the strong coronal magnetic fields and then carry a finite azimuthal velocity component into interplanetary space, which is responsible for the particle contribution to the angular-momentum transport (Weber & Davis 1967). The azimuthal velocity component U_ϕ of the solar wind decreases with distance from the Sun (assuming a torque-free ballistic trajectory, $U_\phi \propto 1/r$), making measurements of U_ϕ at large heliocentric distances particularly difficult. However, observations of cometary tails suggest non-radial solar-wind velocities (Brandt & Heise 1970), and even early *in situ* measurements at 1 au have been used to estimate the Sun's angular-momentum loss (Hundhausen et al. 1970; Lazarus & Goldstein 1971).

As the solar wind accelerates from velocities near zero in the Sun's rest frame up to super-sonic, super-Alfvénic velocities, it must pass two critical distances: the distance r_S at which the outflow speed crosses the local sound speed, and the distance r_A at which the outflow speed crosses the local Alfvén speed (Parker 1958). Their locations generally depend on heliolatitude and undergo variations depending on the properties of the wind's source regions. The sonic and Alfvénic Mach numbers cross the value of unity at these locations, respectively. The heliocentric distance r_β, at which the local thermal pressure in the particles is equal to the energy density in the local magnetic field, is a third important critical distance. All of these critical radii are key predictions of solar-wind models and important for our understanding of the acceleration of the solar wind.

Parker Solar Probe and *Solar Orbiter* are the latest additions to the fleet of solar and solar-wind-observing missions (Fox et al. 2016; Müller et al. 2020). Both missions carry modern instrumentation into the inner heliosphere to measure the particles and the electromagnetic fields of the solar wind *in situ* and monitor the solar-wind outflow remotely. Over the coming years, their observations will improve our understanding of the solar wind at different heliocentric distances and heliolatitudes during solar-minimum and solar-maximum conditions. The goal of our study is the use of radial conservation laws for flux quantities relating to the mass, momentum, energy, and angular momentum of the solar wind to understand their heliolatitudinal variations. Since these quantities are independent of heliocentric distance under a set of assumptions, we use data from *Ulysses* to study their dependence on heliolatitude and solar cycle alone. Within the validity of our assumptions, these measurements serve as contextual information and predictions for the global solar-wind behaviour encountered by *Parker Solar Probe* and *Solar Orbiter*. In addition, we use our scaling parameters to estimate the scaled Alfvénic and sonic Mach numbers as well as the critical radii r_A, r_S, and r_β as functions of heliolatitude based on the *Ulysses* data during solar minimum and solar maximum. In the future, these scaling laws will be refined with data from *Parker Solar Probe* and *Solar Orbiter*, once both missions have explored a wider range of heliocentric distances and heliolatitudes.

2 FLUID EQUATIONS AND CONSERVATION LAWS

For simplicity, the solar wind is described here as a mostly proton–electron plasma[1] with isotropic pressure under the influence of electromagnetic fields. A fluid approach is valid on spatial and temporal scales greater than the characteristic kinetic plasma scales as long as high-order velocity moments of the particle distribution functions can be neglected. We use the proton-fluid continuity equation

$$\frac{\partial N}{\partial t} + \nabla \cdot (N\boldsymbol{U}) = 0, \tag{1}$$

and the proton-fluid momentum equation with isotropic, scalar pressure

$$NM\left[\frac{\partial \boldsymbol{U}}{\partial t} + (\boldsymbol{U}\cdot\nabla)\boldsymbol{U}\right] = -\nabla P + NQ\left(\boldsymbol{E} + \frac{1}{c}\boldsymbol{U}\times\boldsymbol{B}\right) + NM\boldsymbol{g}, \tag{2}$$

where N is the proton density, $\boldsymbol{U}$ is the proton bulk velocity, M is the proton mass, P is the proton pressure, Q is the proton charge, $\boldsymbol{E}$ is the electric field, c is the speed of light, $\boldsymbol{B}$ is the magnetic field, and $\boldsymbol{g}$ is the gravitational acceleration. The electron-fluid equation, neglecting all terms proportional to the electron mass m, is given by

$$-\nabla p + nq\left(\boldsymbol{E} + \frac{1}{c}\boldsymbol{u}\times\boldsymbol{B}\right) = 0, \tag{3}$$

where p is the electron pressure, n and q are the electron number density and charge, and $\boldsymbol{u}$ is the electron bulk velocity. We combine equations (2) and (3) to eliminate $\boldsymbol{E}$. Evoking quasi-neutrality ($N \approx n$), we use the definition of the current density

$$\boldsymbol{j} = NQ\boldsymbol{U} + nq\boldsymbol{u} \tag{4}$$

to obtain

$$NM\left[\frac{\partial \boldsymbol{U}}{\partial t} + (\boldsymbol{U}\cdot\nabla)\boldsymbol{U}\right] = -\nabla(P+p) + \frac{1}{c}\boldsymbol{j}\times\boldsymbol{B} + NM\boldsymbol{g}. \tag{5}$$

Furthermore, we use Ampère's law, $\nabla\times\boldsymbol{B} = 4\pi\boldsymbol{j}/c$, to simplify the remaining electromagnetic force terms, and assume steady-state conditions ($\partial/\partial t = 0$), leading to

$$NM(\boldsymbol{U}\cdot\nabla)\boldsymbol{U} = -\nabla(P+p) - \frac{\nabla\boldsymbol{B}^2}{8\pi} + \frac{(\boldsymbol{B}\cdot\nabla)\boldsymbol{B}}{4\pi} + NM\boldsymbol{g}. \tag{6}$$

We now transform equations (1) and (6) into spherical coordinates. Equation (1) then yields

$$\frac{1}{r^2}\frac{\partial}{\partial r}(r^2 N U_r) + \frac{1}{r\sin\theta}\frac{\partial}{\partial\theta}(NU_\theta\sin\theta) + \frac{1}{r\sin\theta}\frac{\partial}{\partial\phi}(NU_\phi) = 0, \tag{7}$$

where θ is the polar angle and ϕ is the azimuthal angle. In our convention, the heliolatitude λ relates to θ through $\lambda = 90^\circ - \theta$. The radial component of equation (6) is given by

$$\begin{aligned} NM\left(U_r\frac{\partial U_r}{\partial r} + \frac{U_\theta}{r}\frac{\partial U_r}{\partial\theta} + \frac{U_\phi}{r\sin\theta}\frac{\partial U_r}{\partial\phi} - \frac{U_\theta^2+U_\phi^2}{r}\right) \\ = -\frac{\partial}{\partial r}\left(P + p + \frac{\boldsymbol{B}^2}{8\pi}\right) + \frac{1}{4\pi}\left(B_r\frac{\partial B_r}{\partial r} + \frac{B_\theta}{r}\frac{\partial B_r}{\partial\theta} \right. \\ \left. + \frac{B_\phi}{r\sin\theta}\frac{\partial B_r}{\partial\phi} - \frac{B_\theta^2+B_\phi^2}{r}\right) - NMg, \end{aligned} \tag{8}$$

[1]This approach neglects the contribution from α-particles, which we discuss in Section 4.

its polar component by

$$NM\left(U_r\frac{\partial U_\theta}{\partial r}+\frac{U_\theta}{r}\frac{\partial U_\theta}{\partial\theta}+\frac{U_\phi}{r\sin\theta}\frac{\partial U_\theta}{\partial\phi}+\frac{U_rU_\theta}{r}-\frac{U_\phi^2\cot\theta}{r}\right)$$
$$=-\frac{1}{r}\frac{\partial}{\partial\theta}\left(P+p+\frac{\boldsymbol{B}^2}{8\pi}\right)+\frac{1}{4\pi}\left(B_r\frac{\partial B_\theta}{\partial r}+\frac{B_\theta}{r}\frac{\partial B_\theta}{\partial\theta}+\frac{B_\phi}{r\sin\theta}\frac{\partial B_\theta}{\partial\phi}+\frac{B_rB_\theta}{r}-\frac{B_\phi^2\cot\theta}{r}\right), \quad (9)$$

and its azimuthal component by

$$NM\left(U_r\frac{\partial U_\phi}{\partial r}+\frac{U_\theta}{r}\frac{\partial U_\phi}{\partial\theta}+\frac{U_\phi}{r\sin\theta}\frac{\partial U_\phi}{\partial\phi}+\frac{U_rU_\phi}{r}+\frac{U_\phi U_\theta\cot\theta}{r}\right)$$
$$=-\frac{1}{r\sin\theta}\frac{\partial}{\partial\phi}\left(P+p+\frac{\boldsymbol{B}^2}{8\pi}\right)+\frac{1}{4\pi}\left(B_r\frac{\partial B_\phi}{\partial r}+\frac{B_\theta}{r}\frac{\partial B_\phi}{\partial\theta}+\frac{B_\phi}{r\sin\theta}\frac{\partial B_\phi}{\partial\phi}+\frac{B_rB_\phi}{r}+\frac{B_\phi B_\theta\cot\theta}{r}\right). \quad (10)$$

We now assume azimuthal symmetry ($\partial/\partial\phi=0$). Although the observed solar wind exhibits a non-zero polar component U_θ of the bulk velocity and a non-zero polar component B_θ of the magnetic field at times, we assume that $U_\theta=B_\theta=0$ on average as in the Parker (1958) model. The condition $\nabla\cdot\boldsymbol{B}=0$ under our assumptions reduces to

$$\frac{\partial}{\partial r}(r^2B_r)=0. \quad (11)$$

Likewise, continuity according to equation (7) simplifies to

$$\frac{\partial\mathcal{F}_m}{\partial r}=0, \quad (12)$$

where

$$\mathcal{F}_m=r^2NMU_r \quad (13)$$

is the radial mass flux per steradian. The momentum equations in equations (8) through (10) simplify to

$$NM\left(U_r\frac{\partial U_r}{\partial r}-\frac{U_\phi^2}{r}\right)=-\frac{\partial}{\partial r}(P+p)-\frac{1}{r^2}\frac{\partial}{\partial r}\left(r^2\frac{B_\phi^2}{8\pi}\right)-NMg, \quad (14)$$

$$NMU_\phi^2=\frac{1}{4\pi}B_\phi^2, \quad (15)$$

and

$$NM\left(U_r\frac{\partial U_\phi}{\partial r}+\frac{U_rU_\phi}{r}\right)=\frac{1}{4\pi}\left(B_r\frac{\partial B_\phi}{\partial r}+\frac{B_rB_\phi}{r}\right). \quad (16)$$

By combining equation (12) with equations (14) and (15), we find momentum conservation in the form

$$\frac{\partial\mathcal{F}_p}{\partial r}=-r^2\frac{\partial}{\partial r}\left(P+p+\frac{B_\phi^2}{8\pi}\right)-NMGM_\odot, \quad (17)$$

where

$$\mathcal{F}_p=r^2NMU_r^2 \quad (18)$$

is the radial kinetic momentum flux per steradian, G is the gravitational constant, and $M_\odot$ is the Sun's mass. The right-hand side of equation (17) is zero if the solar wind is 'coasting' without radial acceleration, which is a reasonable assumption for heliocentric distances greater than about 0.3 au, especially in fast wind (Marsch & Richter 1984). Slow wind, however, still experiences some acceleration to distances $\gtrsim$1 au (Schwenn et al. 1981). Although this acceleration effect is small, we urge caution when extending our framework into the inner heliosphere. Even if the coasting approximation (i.e. $\mathcal{F}_\mathrm{p}=$ constant) is not fulfilled at the location of the measurement, $\mathcal{F}_\mathrm{p}$ describes the radial component of the particle momentum at this location; however, the scaling of this quantity to different radial distances requires the inclusion of the right-hand side of equation (17).

Under the same assumptions, we find that

$$\frac{\partial}{\partial r}\left[r^2NMU_r\left(\frac{\boldsymbol{U}^2}{2}+\frac{\gamma}{\gamma-1}\frac{P+p}{NM}-\frac{GM_\odot}{r}\right)\right]=\frac{r}{4\pi}(U_\phi B_r-U_rB_\phi)\frac{\partial}{\partial r}(rB_\phi), \quad (19)$$

where γ is the polytropic index (assumed to be equal for protons and electrons). In the derivation of equation (19), we use the polytopic assumption for both protons and electrons:

$$P\propto N^\gamma \quad (20)$$

and

$$p\propto n^\gamma. \quad (21)$$

We note that equation (19) can be easily extended to account for different polytropic indices for protons and electrons. In order to simplify the right-hand side of equation (19), we evoke the frozen-in condition of the magnetic field (Parker 1958). In a frame that co-rotates with the Sun, the magnetic field lines are parallel to $\boldsymbol{U}$ (Weber & Davis 1967; Mestel 1968; Verscharen et al. 2015). This condition leads to

$$\frac{B_\phi}{B_r}=\frac{U_\phi-\Omega_\odot r\sin\theta}{U_r}, \quad (22)$$

where $\Omega_\odot$ is the Sun's angular rotation frequency, which we assume to be constant for all θ. From equation (22), we find the useful identity

$$r(U_\phi B_r-U_rB_\phi)=r^2B_r\Omega_\odot\sin\theta=\text{constant}, \quad (23)$$

where the second equality follows from equation (11). This relationship allows us to simplify the right-hand side of equation (19) so that the energy-conservation law yields

$$\frac{\partial\mathcal{F}_E}{\partial r}=0, \quad (24)$$

where

$$\mathcal{F}_E=r^2NMU_r\left(\frac{\boldsymbol{U}^2}{2}+\frac{\gamma}{\gamma-1}\frac{P+p}{NM}-\frac{GM_\odot}{r}-\frac{rB_rB_\phi}{4\pi NMU_r}\Omega_\odot\sin\theta\right) \quad (25)$$

is the radial energy flux per steradian.

By combining equations (11) and (12) with equation (16), we furthermore identify angular-momentum conservation in the form

$$\frac{\partial\mathcal{F}_L}{\partial r}=0, \quad (26)$$

where

$$\mathcal{F}_L=r^3NMU_rU_\phi-r^3\frac{B_rB_\phi}{4\pi}. \quad (27)$$

The quantities $\mathcal{F}_m$, $\mathcal{F}_p$ (within the coasting approximation), $\mathcal{F}_E$, and $\mathcal{F}_L$ are constant with heliocentric distance. We note that, albeit useful for the description of averaged and global-scale variations, this model ignores any variations due to asymmetries, stream interactions, and natural fluctuations (for a further discussion of these effects, see Section 4).

Table 1. Summary of our measurement results. We show the mean values, minimum values, and maximum values of the quantities illustrated in Figs 1 through 9 for the three fast latitudinal scans (FLSs). The given error bars of the mean values represent the calculated standard errors of the mean.

Quantity	FLS1 (solar minimum)			FLS2 (solar maximum)			FLS3 (solar minimum)		
	Mean	Min	Max	Mean	Min	Max	Mean	Min	Max
$\mathcal{F}_m$ (10^{-16} au^2 g cm^{-2} s^{-1} sr^{-1})	3.549 ± 0.069	1.75	11.06	4.486 ± 0.169	0.680	21.30	2.682 ± 0.082	0.958	15.44
$\mathcal{F}_p$ (10^{-8} au^2 g cm^{-1} s^{-2} sr^{-1})	2.426 ± 0.029	0.739	4.04	2.075 ± 0.076	0.349	9.81	1.705 ± 0.038	0.542	7.97
$\mathcal{F}_E$ (au^2 g s^{-3} sr^{-1})	0.913 ± 0.015	0.166	1.35	0.554 ± 0.025	0.076	2.64	0.601 ± 0.014	0.097	2.25
$\mathcal{F}_L$ (10^{-9} au^3 g cm^{-1} s^{-2} sr^{-1})*	1.162 ± 0.037	0.060	1.94	0.715 ± 0.074	0.001	3.58	0.765 ± 0.026	0.018	1.38
$\tilde{M}_A$	18.892 ± 1.426	7.23	343.43	21.339 ± 1.597	4.21	200.44	22.300 ± 0.541	6.54	99.00
r_A ($R_\odot$)	12.080 ± 0.236	0.128	26.00	12.766 ± 0.522	0.008	47.15	9.504 ± 0.221	0.289	28.31
$\tilde{M}_S$	11.409 ± 0.057	7.87	16.93	11.594 ± 0.148	7.04	18.72	12.079 ± 0.079	7.69	17.96
r_S ($R_\odot$)	0.309 ± 0.004	0.104	0.819	0.346 ± 0.012	0.079	1.11	0.273 ± 0.006	0.088	0.871
r_β (au)†	0.552 ± 0.028	0.011	3.18	0.658 ± 0.052	0.000	4.07	0.488 ± 0.048	0.036	6.69

Note. *The statistics for $\mathcal{F}_L$ only include those times when $\mathcal{F}_L > 0$. †The statistics for r_β only include those times when $r_\beta > 0$.

3 DATA ANALYSIS

We use 30-h averages of the proton and magnetic-field data recorded by *Ulysses* during its three polar orbits. We choose an average interval of 30 h to sample over time-scales that are greater than the typical correlation time of the ubiquitous solar-wind fluctuations (typically of order a few hours; Matthaeus & Goldstein 1982; Bruno & Dobrowolny 1986; Tu & Marsch 1995; D'Amicis et al. 2010; Bruno & Carbone 2013). At the same time, this averaging interval is short enough to avoid significant variations in *Ulysses'* heliolatitude during the recording of each data point in our averaged data set. The proton measurements were recorded by the Solar Wind Observations Over the Poles of the Sun (SWOOPS) instrument (Bame et al. 1992). The magnetic-field measurements were recorded by the Magnetic Field experiment (Balogh et al. 1992). In order to visualize the differences between solar minimum and solar maximum conditions, we only use data from *Ulysses'* three fast heliolatitude scans. The first scan occurred during solar minimum, the second scan occurred during solar maximum, and the third scan occurred during the following (deep) solar minimum (McComas et al. 2008). We select data from DOY 256 in 1994 until DOY 213 in 1995 (known as Fast Latitude Scan 1, FLS1) and data from DOY 38 in 2007 until DOY 13 in 2008 (known as Fast Latitude Scan 3, FLS3), and label these data as 'solar minimum'. We select data from DOY 329 in 2000 until DOY 285 in 2001 (known as Fast Latitude Scan 2, FLS2) and label these data as 'solar maximum'. During these time intervals, *Ulysses'* eccentric orbit brought the spacecraft to heliocentric distances between 1.34 au at the perihelia and 2.37 au at the furthest polar pass. We summarise our results in Table 1.

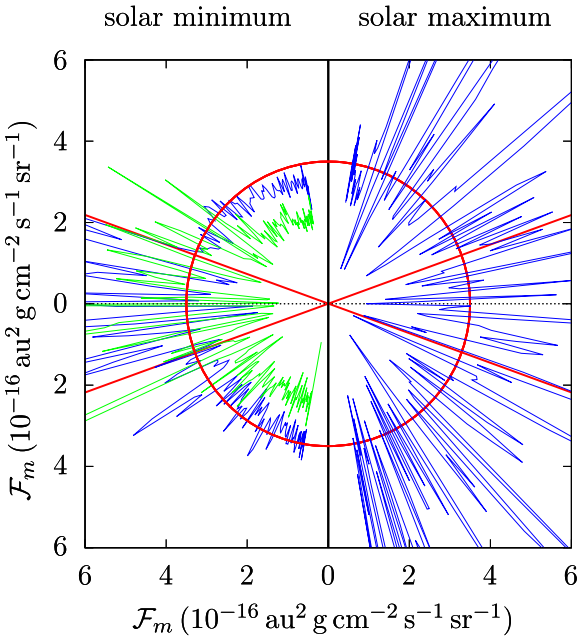

Figure 1. Polar plot of the radial mass flux per steradian $\mathcal{F}_m$. The polar angle represents the heliolatitude λ at which *Ulysses* recorded the measurement. The distance from the centre of the plot describes the local value of $\mathcal{F}_m$. The red lines indicate $\lambda = \pm 20°$. The red circle has a radius of 3.5×10^{-16} au^2 g cm^{-2} s^{-1} sr^{-1}. The left half of the figure shows conditions during solar minimum from FLS1 (blue) and FLS3 (green), and the right half of the figure shows conditions during solar maximum from FLS2 (blue).

3.1 Mass, momentum, energy, and angular-momentum flux

In Fig. 1, we show a polar plot of the radial mass flux per steradian $\mathcal{F}_m$ based on the *Ulysses* measurements. The polar angle in this diagram and in the following diagrams illustrates the heliolatitude at which the measurement was taken. The red lines indicate the heliolatitudes of ±20°, which McComas et al. (2000) identify as the separation between slow equatorial streamer-belt wind and fast polar coronal-hole wind during solar minimum. The red circle indicates a constant value of $\mathcal{F}_m = 3.5 \times 10^{-16}$ au^2 g cm^{-2} s^{-1} sr^{-1} and is meant as a help to guide the eye. During solar minimum, $\mathcal{F}_m$ varies between about 1×10^{-16} and 15×10^{-16} au^2 g cm^{-2} s^{-1} sr^{-1} in the equatorial region, while it is steadier over the polar regions beyond ±20° at a value of about 3.5×10^{-16} au^2 g cm^{-2} s^{-1} sr^{-1} during FLS1. The polar mass flux is lower at a value of about 2.2×10^{-16} au^2 g cm^{-2} s^{-1} sr^{-1} during FLS3. During solar maximum, $\mathcal{F}_m$ exhibits large variations consistent with the larger variability of the solar-wind source regions. The maximum value during solar maximum is about 2.1×10^{-15} au^2 g cm^{-2} s^{-1} sr^{-1}, which is almost by a factor of 10 greater than the average value over polar regions during solar minimum. The clear separation between equatorial and polar wind vanishes during solar maximum.

We show the polar plot of the radial particle momentum flux per steradian $\mathcal{F}_p$ in Fig. 2 for solar-minimum and solar-maximum conditions. During solar minimum, $\mathcal{F}_p$ presents variations between about 0.5×10^{-8} and 8×10^{-8} au^2 g cm^{-1} s^{-2} sr^{-1} at equatorial heliolatitudes below ±20°. Outside the equatorial region, $\mathcal{F}_p$ is almost independent of heliolatitude at a value of approximately 2.5×10^{-8} au^2 g cm^{-1} s^{-2} sr^{-1} during FLS1 and at a value of approximately 1.7×10^{-8} au^2 g cm^{-1} s^{-2} sr^{-1} during FLS3. Like in the case of $\mathcal{F}_m$, also $\mathcal{F}_p$ shows a strong variation during solar

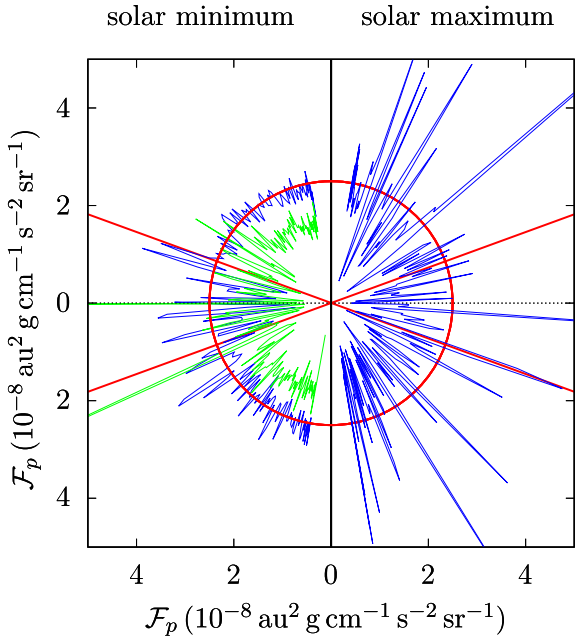

Figure 2. Polar plot of the radial particle momentum flux per steradian $\mathcal{F}_p$ during solar minimum (left half, FLS1 in blue, FLS3 in green) and solar maximum (right half, FLS2). The format of this plot is the same as in Fig. 1. The red circle has a radius of 2.5×10^{-8} au^2 g cm^{-1} s^{-2} sr^{-1}.

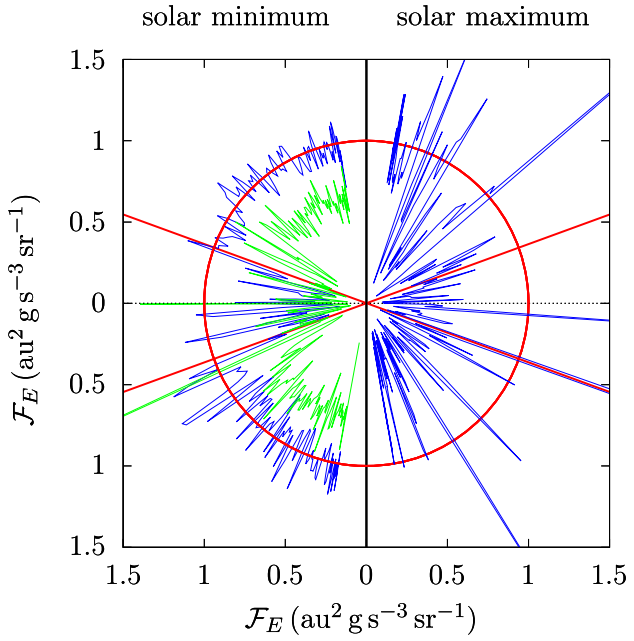

Figure 3. Polar plot of the radial energy flux per steradian $\mathcal{F}_E$ during solar minimum (left half, FLS1 in blue, FLS3 in green) and solar maximum (right half, FLS2). We use $\gamma = 5/3$ and assume that $p = P$. The format of this plot is the same as in Fig. 1. The red circle has a radius of 1 au^2 g s^{-3} sr^{-1}.

maximum between values from less than 3×10^{-9} to almost 10^{-7} au^2 g cm^{-1} s^{-2} sr^{-1} at times. At equatorial heliolatitudes, the average $\mathcal{F}_p$ does not differ much between solar minimum and solar maximum, although its variability is greater during solar maximum.

Fig. 3 shows our polar plot of the radial energy flux per steradian $\mathcal{F}_E$. During solar minimum, $\mathcal{F}_E$ exhibits a significant difference

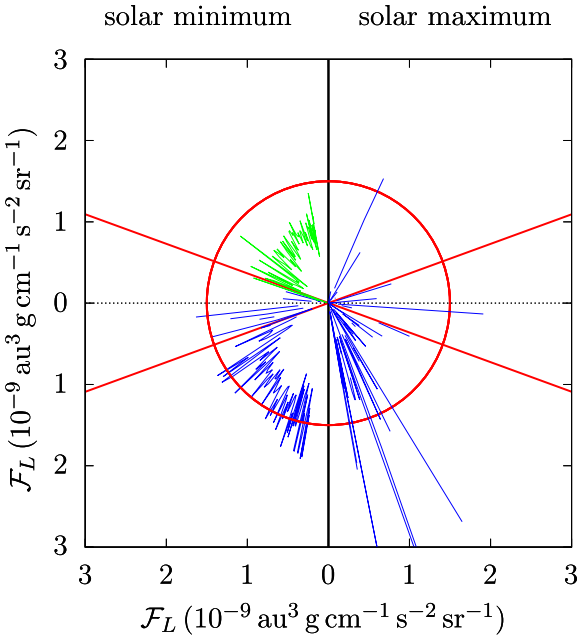

Figure 4. Polar plot of the radial angular-momentum flux per steradian $\mathcal{F}_L$ during solar minimum (left half, FLS1 in blue, FLS3 in green) and solar maximum (right half, FLS2). We only plot $\mathcal{F}_L$ if $\mathcal{F}_L > 0$. The format of this plot is the same as in Fig. 1. The red circle has a radius of 1.5×10^{-9} au^3 g cm^{-1} s^{-2} sr^{-1}.

between equatorial and polar regions. Near the equator between $\lambda = \pm 20^\circ$, we observe $\mathcal{F}_E$ between about 0.1 and 2.2 au^2 g s^{-3} sr^{-1}. Outside the equatorial heliolatitudes, we observe an average value of about 1 au^2 g s^{-3} sr^{-1} during FLS1 and about 0.7 au^2 g s^{-3} sr^{-1} during FLS3, independent of λ. During solar maximum, $\mathcal{F}_E$ expectedly shows a larger variability between values from below 0.1 to above 2.6 au^2 g s^{-3} sr^{-1}. At the location of the measurement, $\mathcal{F}_E$ is dominated by the kinetic-energy contribution of the protons.

We show the polar plot of the radial angular-momentum flux per steradian $\mathcal{F}_L$ in Fig. 4. Due to pointing uncertainties in the *Ulysses* data set (for details, see Section 4), the measurement of U_ϕ is prone to a much larger uncertainty than the measurement of U_r. We therefore only plot $\mathcal{F}_L$ when $\mathcal{F}_L > 0$. Due to the data gaps when $\mathcal{F}_L < 0$, it is impossible to define a meaningful average value for $\mathcal{F}_L > 0$ at Northern heliolatitudes above the equatorial plane during FLS1 and at Southern heliolatitudes below the equatorial plane during FLS3. Even the equatorial values need to be treated with caution. During solar minimum, we find that $\mathcal{F}_L$ is approximately 1.2×10^{-9} au^3 g cm^{-1} s^{-2} sr^{-1} in the Southern polar region (FLS1) and approximately 0.8×10^{-9} au^3 g cm^{-1} s^{-2} sr^{-1} in the Northern polar region (FLS3). During solar maximum, its value varies between 6×10^{-13} au^3 g cm^{-1} s^{-2} sr^{-1} and about 3.6×10^{-9} au^3 g cm^{-1} s^{-2} sr^{-1}. However, we re-iterate that these values need to be treated with caution based on the pointing uncertainty of the spacecraft.

3.2 Alfvénic Mach number and the Alfvén radius

In this section, we derive the value of the Alfvénic Mach number scaled to a heliocentric distance of 1 au and the location of the Alfvén radius as functions of heliolatitude. For this calculation, we require a scaling law for the magnetic field $\boldsymbol{B}$. Throughout this work, we use the tilde symbol to indicate a quantity that has been scaled to its value at a heliocentric distance of 1 au. Using assumptions consistent with

ours, Parker (1958) provides expressions for the averaged global-scale heliospheric magnetic field as

$$B_r(r) = B_r(r_0)\left(\frac{r_0}{r}\right)^2, \tag{28}$$

$$B_\theta = 0, \tag{29}$$

and

$$B_\phi(r) = B_r(r)\frac{\Omega_\odot \sin\theta}{U_r}(b-r), \tag{30}$$

where r_0 is any arbitrary reference distance from the Sun and b is the effective source-surface radius. In order to scale the measured magnetic field from the *Ulysses* data set to its value at 1 au, we assume that the averaged heliospheric magnetic field follows, to first order, the Parker magnetic field. Since $b \ll r$, we approximate equation (30) as

$$B_\phi(r) \approx B_\phi(r_0)\left(\frac{r_0}{r}\right). \tag{31}$$

Using equations (28) and (31), we approximate the magnitude of the scaled magnetic field at a heliocentric distance of 1 au as

$$\tilde{B} = \left(\frac{r}{1\,\mathrm{au}}\right)\sqrt{\left(\frac{r}{1\,\mathrm{au}}\right)^2 B_r^2 + B_\phi^2}, \tag{32}$$

where B_r and B_ϕ are the measured magnetic-field components at the heliocentric distance r, and r is the heliocentric distance of the measurement location. Assuming that the proton bulk velocity remains independent of r for $r \gtrsim 1$ au, equation (12) suggests that $N \propto r^{-2}$, allowing us to define the scaled proton density at a heliocentric distance of 1 au as

$$\tilde{N} = N\left(\frac{r}{1\,\mathrm{au}}\right)^2. \tag{33}$$

Using equations (32) and (33), we define the scaled Alfvén speed at a heliocentric distance of 1 au as

$$\tilde{v}_\mathrm{A} = \frac{\tilde{B}}{\sqrt{4\pi\tilde{N}M}}. \tag{34}$$

Likewise, we define the scaled Alfvénic Mach number at a heliocentric distance of 1 au as

$$\tilde{M}_\mathrm{A} = \frac{U_r}{\tilde{v}_\mathrm{A}}, \tag{35}$$

again relying on the assumption that U_r is independent of r for $r \gtrsim 1$ au.

We show our polar plot of the scaled Alfvénic Mach number $\tilde{M}_\mathrm{A}$ in Fig. 5. The scaled solar wind at 1 au is super-sonic ($\tilde{M}_\mathrm{A} > 1$) at all heliolatitudes and both during solar minimum and solar maximum. During solar minimum, $\tilde{M}_\mathrm{A}$ exhibits more variation at equatorial heliolatitudes with values between 7 and 343. Outside the equatorial region, the solar-minimum value of $\tilde{M}_\mathrm{A}$ varies between 12 and 30 during FLS1 and between 13 and 57 during FLS3. On average, $\tilde{M}_\mathrm{A}$ is greater during FLS3 than during FLS1. We observe a slight increase of $\tilde{M}_\mathrm{A}$ with increasing $|\lambda|$ even above $\pm 20°$. During solar maximum, $\tilde{M}_\mathrm{A}$ exhibits a large variability between values from about 4 to extreme cases with values over 200 at times. During solar maximum, the maxima and the variations in $\tilde{M}_\mathrm{A}$ are greater in polar regions than near the equator.

The Alfvén radius r_A is generally defined as the heliocentric distance r, at which the radial proton bulk velocity fulfills

$$U_r = v_\mathrm{A}(r), \tag{36}$$

where $v_\mathrm{A}(r)$ is the local Alfvén speed. Our scaling assumptions require that $b \ll r$ and that U_r is constant with distance from the Sun as in the original Parker (1958) model for the interplanetary magnetic field. We now extend the assumption that $\partial U_r/\partial r = 0$ to all distances $r \gtrsim r_\mathrm{A}$. We recognize that this assumption is sometimes violated. It allows us, however, to set a reasonable upper limit on U_r as a function of r. As long as the actual $U_r(r_\mathrm{A})$ is less than the measured U_r at distance r and v_A is a monotonic function of r, the extension of our scaling relations in equations (32) and (33) to $r = r_\mathrm{A}$ provides us then with a lower-limit estimate for the Alfvén radius. Using the condition in equation (36), we find

$$r_\mathrm{A} = r\sqrt{\frac{B_r^2}{4\pi N M U_r^2 - B_\phi^2}}, \tag{37}$$

where B_r, B_ϕ, N, and U_r are the measured quantities at heliocentric distance r. We show the polar plot of the estimated Alfvén radius r_A according to equation (37) in Fig. 6. During solar minimum, r_A exhibits more variation in the equatorial region compared to the polar region. Within heliolatitudes of $\pm 20°$ of the equator, r_A varies between about 0.1 and 28 $\mathrm{R}_\odot$. Polewards from this equatorial region, we find r_A between about 7 and 16 $\mathrm{R}_\odot$ with a mean of approximately 12 $\mathrm{R}_\odot$ during FLS1. During FLS3, r_A is on average smaller in the polar regions with a mean value of approximately 10 $\mathrm{R}_\odot$. As expected, the value of r_A exhibits more variability during solar maximum between values from less than 0.01 to 47 $\mathrm{R}_\odot$ in extreme cases. We note that values of $r_\mathrm{A} < 1\,\mathrm{R}_\odot$ are unphysical as these would lie within the sphere of the Sun.

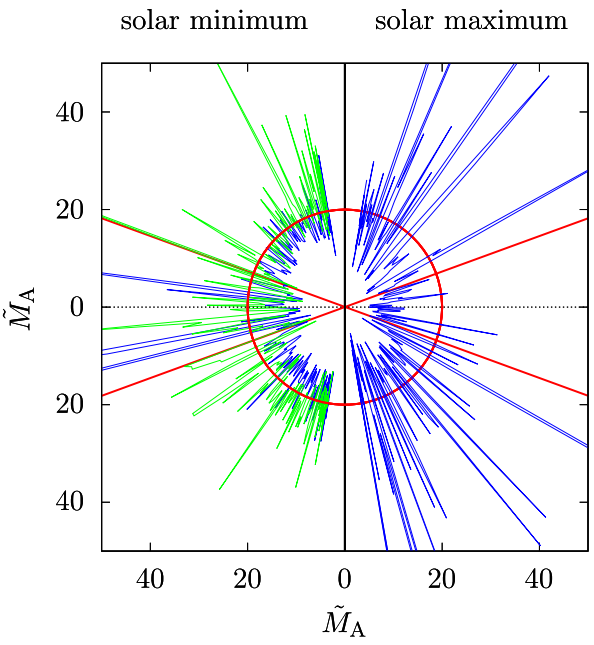

Figure 5. Polar plot of the scaled Alfvénic Mach number $\tilde{M}_\mathrm{A}$ at $r = 1$ au during solar minimum (left half, FLS1 in blue, FLS3 in green) and solar maximum (right half, FLS2). The format of this plot is the same as in Fig. 1. The red circle has a radius of 20.

3.3 Sonic Mach number, the sonic radius, and the $\beta = 1$ radius

In this section, we derive the value of the sonic Mach number scaled to a heliocentric distance of 1 au, the location of the sonic radius, and the location of the $\beta = 1$ radius as functions of heliolatitude. For this calculation, we require a scaling law for the proton temperature T. Fits to the proton temperature profiles observed by *Ulysses* during its first polar orbit reveal a temperature dependence on

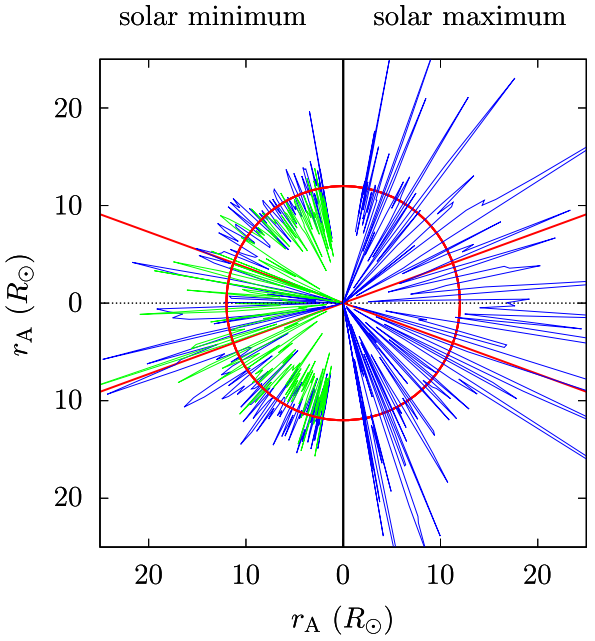

Figure 6. Polar plot of the estimated Alfvén radius r_A based on the scaled magnetic field and proton density during solar minimum (left half, FLS1 in blue, FLS3 in green) and solar maximum (right half, FLS2). The values of r_A give lower estimates for the Alfvén radius. We only plot r_A if $r_A > 0$. The format of this plot is the same as in Fig. 1. The red circle has a radius of $12\,R_\odot$.

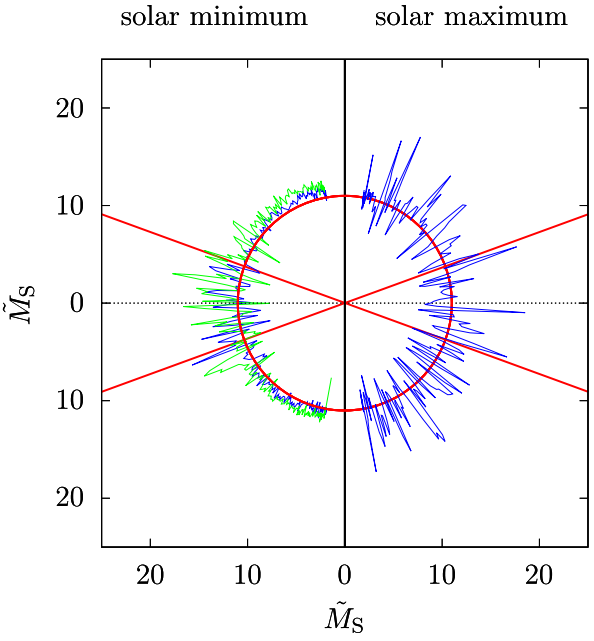

Figure 7. Polar plot of the scaled sonic Mach number $\tilde{M}_S$ at $r = 1$ au during solar minimum (left half, FLS1 in blue, FLS3 in green) and solar maximum (right half, FLS2). The format of this plot is the same as in Fig. 1. The red circle has a radius of 11.

heliocentric distance and heliolatitude of the form (McComas et al. 2000)

$$T = \left[2.58 \times 10^5\,\mathrm{K} + (223\,\mathrm{K})\left(\frac{\lambda}{1^\circ}\right)\right]\left(\frac{r}{1\,\mathrm{au}}\right)^{-1.02} \tag{38}$$

at high heliolatitudes ($|\lambda| \geq 36^\circ$). The temperature distribution at equatorial heliolatitudes during solar minimum and, in general, during solar maximum is more complex (McComas et al. 2002). Nevertheless, we apply the power-law scaling in equation (38) to approximately scale T at the location of measurement back to its value at 1 au as

$$\tilde{T} = T\left(\frac{r}{1\,\mathrm{au}}\right)^{1.02}. \tag{39}$$

The *Ulysses* data set provides us with proton temperature measurements achieved in two different ways: one data product corresponds to the integrated second velocity moment of the 3D velocity distribution function. The other data product corresponds to the sum of the second-order moments of 1D energy spectra, avoiding any channels above the proton peak to avoid contamination by α-particles. These one-dimensional spectra are calculated as the sum of the measurements over all angles at each fixed energy. Unless the solar-wind temperature T assumes extreme values, the integrated second velocity moment of the 3D velocity distribution function is expected to provide an upper limit on T. In these cases, the sum of the second-order moments of the 1D energy spectra is expected to provide a lower limit on T. We use the arithmetic mean of the time averages of both data products as our value of T.

We define the scaled sound speed at a heliocentric distance of 1 au as

$$\tilde{c}_S = \sqrt{\frac{\gamma k_B \tilde{T}}{M}}, \tag{40}$$

where k_B is the Boltzmann constant. For the sake of simplicity, we set $\gamma = 5/3$. This definition allows us to introduce the scaled sonic Mach number at a heliocentric distance of 1 au as

$$\tilde{M}_S = \frac{U_r}{\tilde{c}_S} \tag{41}$$

under the assumption that $\partial U_r/\partial r = 0$ at distances $r \gtrsim 1$ au. Fig. 7 displays the polar plot of the scaled sonic Mach number $\tilde{M}_S$. The value of $\tilde{M}_S$ shows the least relative variability compared to the other quantities shown in this work throughout the three polar passes that we study. During solar minimum, $\tilde{M}_S$ varies between 8 and 18. At $|\lambda| > 20^\circ$, $\tilde{M}_S$ is approximately constant at a value of 11 during FLS1 and at a value of 12 during FLS3. During solar maximum, $\tilde{M}_S$ exhibits moderate variations with values between approximately 7 and 19. The difference between equatorial and polar wind is less pronounced during solar maximum.

Assuming an average radial scaling of T at heliocentric distances < 1 au in addition to the scaling in equation (39), which is valid at heliocentric distances >1 au, allows us to estimate the value of the sonic radius r_S based on the *Ulysses* measurements depending on heliographic latitude in cases when $r_S < 1$ au. The sonic radius is defined as the heliocentric distance r, at which the radial proton bulk velocity fulfills

$$U_r = c_S(r), \tag{42}$$

where $c_S(r)$ is the local sound speed. Like in the case of the Alfvén radius, we apply our assumption that $\partial U_r/\partial r = 0$ to all distances $r \gtrsim r_S$, an assumption that is prone to the same caveats as in the case of r_A. Fits to radial profiles of T measured by *Helios* in fast solar wind reveal (Hellinger et al. 2011)

$$T(r) = 2.5 \times 10^5\,\mathrm{K}\left(\frac{r}{1\,\mathrm{au}}\right)^{-0.74}. \tag{43}$$

Like in the case of our *Ulysses* measurements, the *Helios* proton temperature profiles also depend on the solar-wind speed (Marsch

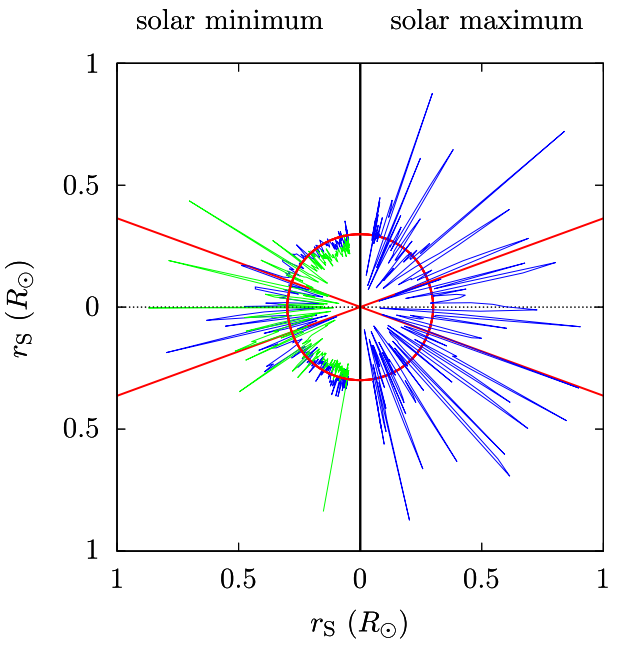

Figure 8. Polar plot of the estimated sonic radius r_S based on the scaled proton temperature during solar minimum (left half, FLS1 in blue, FLS3 in green) and solar maximum (right half, FLS2). The values of r_S give lower estimates for the sonic radius. We only plot r_S if $r_S > 0$. The format of this plot is the same as in Fig. 1. The red circle has a radius of 0.3 $R_\odot$.

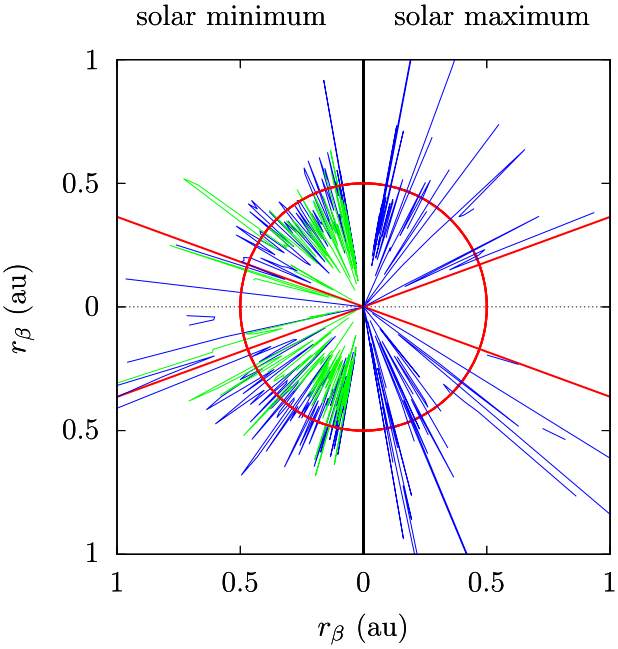

Figure 9. Polar plot of the estimated $\beta = 1$ radius r_β based on the scaled moment profiles during solar minimum (left half, FLS1 in blue, FLS3 in green) and solar maximum (right half, FLS2). We only plot r_β if $r_\beta > 0$. The format of this plot is the same as in Fig. 1. The red circle has a radius of 0.5 au.

et al. 1982b). The power index for the scaling of the perpendicular proton temperature varies from −1.17 in fast wind to −0.9 in slow wind, and the power index for the scaling of the parallel proton temperature varies from −0.69 in fast wind to −1.03 in slow wind. We combine the scaling in equation (39) with the scaling

$$T = \tilde{T}\left(\frac{r}{1\,\mathrm{au}}\right)^{-0.74} \tag{44}$$

according to equation (43) to estimate the r-dependence of the proton temperature from the location of the *Ulysses* measurement to the heliocentric distance r_S. We acknowledge that the assumption of a single power index neglects the differences in the temperature profiles between fast and slow wind and should be seen as an average estimate.

The procedure for the calculation of r_S is as follows. We first calculate $\tilde{T}$ according to equation (39). Then we apply the scaling in equation (44) to achieve an r-dependent value of $T(r)$ in the inner heliosphere. Based on this value, we calculate $c_S(r)$ and evaluate the distance at which equation (42) is fulfilled. This leads to

$$r_S = (1\,\mathrm{au})\,\tilde{M}_S^{-2.70}. \tag{45}$$

As for our estimate of r_A, equation (45) gives a lower limit on the sonic radius due to our assumption that $\partial U_r/\partial r = 0$ at $r \gtrsim r_S$. We show the polar plot of the estimated sonic radius r_S according to equation (45) in Fig. 8. Overall, we observe an increase of r_S with increasing $|\lambda|$ both during solar minimum and solar maximum. During solar minimum, r_S varies between values of about 0.09 and 0.9 $R_\odot$ at equatorial heliolatitudes. At polar heliolatitudes, $r_S \approx 0.3\,R_\odot$ during both FLS1 and FLS3, although the average r_S is slightly smaller during FLS3. During solar maximum, the value of r_S varies between about 0.08 and 1.1 $R_\odot$. We discuss in Section 4 that our assumptions in the derivation of equation (45) are strongly violated at these distances, casting doubt on the reliability of our estimate of r_S. In addition, numerical values of $r_S < 1\,R_\odot$, like for the case of r_A, are clearly unphysical as they lie within the sphere of the Sun.

Lastly, we estimate the radius r_β at which $\beta = 1$, where

$$\beta = \frac{8\pi N k_B T}{B^2} \tag{46}$$

is the ratio between the thermal pressure of the protons and the magnetic energy density. Since r_β can be greater than or less than 1 au, we must account for the different T-scalings according to equations (39) and (44) in the outer and inner heliosphere. The radius r_β then fulfils the conditions

$$B_r^2 + \left(\frac{r_\beta}{r}\right)^2 B_\phi^2 - 8\pi N k_B T \left(\frac{r_\beta}{r}\right)^{0.98} = 0 \tag{47}$$

if $r_\beta > 1$ au and

$$B_r^2 + \left(\frac{r_\beta}{r}\right)^2 B_\phi^2 - 8\pi N k_B T \left(\frac{r_\beta}{r}\right)^{1.26} \left(\frac{r}{1\,\mathrm{au}}\right)^{0.28} = 0 \tag{48}$$

if $r_\beta < 1$ au. We solve this set of conditional equations (47) and (48) numerically for r_β through a Newton-secant method. We ignore all cases in which the solution leads to $r_\beta < 0$. We show the polar plot of the estimated $\beta = 1$ radius r_β according to equations (47) and (48) in Fig. 9. The data gaps in Fig. 9 show that our method at times fails to provide a reliable estimate for r_β in equatorial regions. Under solar-minimum conditions, we find solutions with 0.01 au $< r_\beta <$ 3.2 au in the equatorial plane for some time intervals. We find that r_β assumes average values between about 0.2 and 0.5 au at heliolatitudes polewards of ±20° during solar minimum. During FLS3, r_β is on average less than r_β during FLS1. During solar maximum, r_β varies from 0 to about 4 au. Like in the solar-minimum case, our approach does not always provide us with reliable estimates for r_β near the equatorial plane during solar maximum. We find equatorial solutions with 0.2 au $< r_\beta <$ 2.6 au during maximum conditions.

4 DISCUSSION

Our measurement of the mass flux per steradian $\mathcal{F}_m$ in the ecliptic plane is consistent with earlier measurements (Feldman et al. 1978; McComas et al. 2000; Cranmer, Gibson & Riley 2017; Finley, Matt & See 2018). These observations report that $4\pi r^2 U_r N M \approx 10^{12}\,\mathrm{g\,s^{-1}}$, which corresponds to $\mathcal{F}_m \approx 4 \times 10^{-16}\,\mathrm{au^2\,g\,cm^{-2}\,s^{-1}\,sr^{-1}}$ in our units. In agreement with previous measurements from *Ulysses* during solar minimum (Forsyth et al. 1996b; Goldstein et al. 1996), we find that $\mathcal{F}_m$ is approximately constant for $|\lambda| > 20^\circ$, although we find a slight decrease of $\mathcal{F}_m$ towards the poles during FLS1, especially during the Northern pass at solar minimum (see also McComas et al. 2000). In general, $\mathcal{F}_m$ is by almost 25 per cent smaller during the minimum recorded in FLS3 than during the minimum recorded in FLS1. This finding confirms the extraordinary conditions during the very deep solar minimum that extended into 2009 (McComas et al. 2013). The mass flux is a useful quantity to distinguish solar-wind acceleration models. As pointed out by Holzer & Leer (1980), for instance, a constancy of the mass flux with solar-wind speed would suggest that most of the energy deposition occurs above the Alfvén-critical point. The observed variability in $\mathcal{F}_m$, however, confirms the notion that most of the energy deposition occurs below the critical point. We note that α-particles, which we neglect, can make a substantial contribution ($\lesssim$20 per cent) to the solar-wind mass flux, especially in fast solar wind (Marsch et al. 1982a).

Our estimate for the momentum flux per steradian $\mathcal{F}_p$ is not fully scalable to different r across the heliosphere, since it does not include the contributions from plasma-pressure gradients, magnetic-pressure gradients, and gravity. Although these effects are small at the location of the measurement, we warn that the scaling of $\mathcal{F}_p$ to the inner heliosphere deserves particular attention due to our application of the coasting approximation. Including α-particles, which can make a substantial contribution to the momentum flux of the solar wind, McComas et al. (2000) report a momentum flux of approximately $2.9 \times 10^{-8}\,\mathrm{au^2\,g\,cm^{-1}\,s^{-2}\,sr^{-1}}$ during FLS1 in solar-minimum conditions with a variation of 0.3 per cent per degree in heliolatitude. Our measurements confirm that, both during solar minimum and (to a lesser degree) during solar maximum, the average momentum flux is lower in equatorial regions with only a small variation with heliolatitude in the polar regions (Phillips et al. 1995). We note, however, that, during all FLS orbits, the *Ulysses* spacecraft has a larger latitudinal angular speed in the equatorial regions than in the polar regions. Therefore, the spacecraft may statistically encounter fewer transient events near the equator which potentially skews the measured variability. The deep solar minimum during FLS3 exhibits polar $\mathcal{F}_p$-values that are by about 30 per cent smaller than the average polar $\mathcal{F}_p$ during FLS1. The momentum flux is of particular interest since it represents the solar-wind ram pressure, the key internal driver that determines the shape and extent of the heliosphere at the location of the heliospheric termination shock (McComas et al. 2000; Jokipii 2013).

An earlier measurement of the solar wind's kinetic-energy density based on a combination of data from the *Helios*, *Ulysses*, and *Wind* missions shows that $W = NMU_r U_r^2/2 + NMU_r GM_\odot/R_\odot$ is largely independent of solar-wind speed at a value of approximately $1.5 \times 10^{-3}\,\mathrm{W\,m^{-2}}$ at $r = 1$ au and in the plane of the ecliptic (Le Chat, Issautier & Meyer-Vernet 2012). We note that W depends on r, unlike our $\mathcal{F}_E$, which also includes contributions from the plasma pressure, and the magnetic field. Nevertheless, since these measurements are reported at $r = 1$ au, we can compare W with $\mathcal{F}_E$ by calculating $r^2 W \approx 1.5\,\mathrm{au^2\,g\,s^{-3}\,sr^{-1}}$, which is slightly larger than our reported value. The estimate by Le Chat et al. (2012) includes the required energy for the plasma to leave the Sun's gravitational potential from a distance of $r = 1\,\mathrm{R}_\odot$. Since even for fast wind $GM_\odot/R_\odot \sim U_r^2/2$, this additional contribution to W explains the difference in these two estimates. The contribution of the magnetic field to $\mathcal{F}_E$ is small in agreement with modelling results (Alexander & de La Torre 1995). At the distance at which *Ulysses* measured $\mathcal{F}_E$, the energy flux is dominated by the kinetic-energy flux. An earlier analysis of *Ulysses* data reveals that the equatorial kinetic-energy flux is approximately 30 per cent less than the polar kinetic-energy flux (Phillips et al. 1995) consistent with our results, although this earlier study did not analyse its heliolatitudinal dependence during conditions near solar maximum. The deep solar minimum during FLS3 exhibits a polar energy flux that is by about 34 per cent smaller than the polar energy flux during FLS1.

Due to pointing uncertainties explicitly communicated by the instrument team, *Ulysses* is unable to provide us with a reliable measurement of U_ϕ on the required time-scales. U_ϕ is a key component in the calculation of $\mathcal{F}_L$. Therefore, our polar plot of $\mathcal{F}_L$ in Fig. 4 must be treated with caution. In addition, U_ϕ often exhibits relative variations greater than order unity so that it even assumes negative values in the solar wind. Natural variations due to turbulence or stream-interaction regions cause significant deflections compared to the expected average (Egidi, Pizzella & Signorini 1969; Siscoe, Goldstein & Lazarus 1969). Although time averaging reduces the impact of these natural variations on the determination of the average U_ϕ, the instrumental shortcomings remain. In addition to uncertainties in U_ϕ, the accuracy of $\mathcal{F}_L$ also depends on the average values of B_r and B_ϕ. Although *Ulysses* observations show that the average interplanetary magnetic field largely agrees with Parker's prediction, B_r decreases more slowly and B_ϕ more quickly with heliocentric distance than expected (McComas et al. 2000). These deviations are usually attributed to waves or more complex boundary conditions near the Sun than those assumed in Parker's model (Forsyth et al. 1996a, b). In Section 3.2, we scale the magnetic field towards smaller r assuming the radial scaling according to Parker's model. We expect that our averaging over 30 h removes most of the Alfvénic fluctuations that lead to variations in U_ϕ and B_ϕ around their mean values. Some of the inaccuracies due to complex boundary conditions can be reduced using a more complex model for the interplanetary magnetic field such as the Fisk (1996) model, which accounts for the Sun's differential rotation and the tilt of the Sun's magnetic axis compared to its rotational axis. However, such a more complex treatment is beyond the scope of this work.

Earlier measurements of the Sun's angular-momentum loss provide a value of $\mathcal{F}_L \approx 5 \ldots 10 \times 10^{-10}\,\mathrm{au^3\,g\,cm^{-1}\,s^{-2}\,sr^{-1}}$ (Pizzo et al. 1983; Finley et al. 2018, 2019; Verscharen et al. 2021). Despite the inaccuracies in the *Ulysses* measurement, these values are consistent with our estimates of $\mathcal{F}_L$ in the Southern hemisphere during FLS1, in the Northern hemisphere during FLS3, and during solar maximum (FLS2). The contribution to the angular-momentum flux from α-particles, which we neglect in our estimate, can be significant in the solar wind (Pizzo et al. 1983; Marsch & Richter 1984; Verscharen et al. 2015) and should be included in future studies with spacecraft that provide readily available α-particle data. The partition between the particle contributions and the magnetic-field contributions to $\mathcal{F}_L$ is an important question with implications for solar-wind models. In the early Weber & Davis (1967) model, the field contribution is greater than the particle contribution; however, later measurements show that the partition can be opposite, especially in slow wind (Hundhausen et al. 1970; Marsch & Richter 1984). In typical fast wind, most of the angular-momentum is lost through magnetic stresses, an effect which is expected to be even stronger in

the inner heliosphere (see also Pizzo et al. 1983; Alexander & de La Torre 1995). Likewise, the on average larger pressure anisotropies in the inner heliosphere (Marsch et al. 1982b) contribute to the angular-momentum equation (Hundhausen 1970), even though we neglect their effect in our treatment based on the assumption of a scalar pressure. Due to the limitations in our measurement of U_ϕ, we are unable to determine reliably the partition of these different contributions to the overall angular-momentum loss. In the very inner heliosphere, *Parker Solar Probe* reports an azimuthal flow which is significantly larger than expected by the Weber & Davis (1967) model (Kasper et al. 2019). The source of this large U_ϕ component is still unclear. A stronger effective co-rotation or deflections through, for instance, stream interactions serve as potential explanations (Finley et al. 2020). In this context, a more complex field geometry near the Sun also affects the angular-momentum loss (Finley & Matt 2017), which introduces further dependencies on the solar cycle (Réville & Brun 2017; Finley et al. 2018).

A combination of *Ulysses* measurements with a self-similar solar-wind model finds a scaled Alfvén Mach number $\tilde{M}_\mathrm{A}$ of about 10–20 (Sauty et al. 2005) consistent with our simpler scaling estimate in Section 3.3. The earlier self-similar model, however, suffered from inconsistencies in reproducing observed magnetic-field values at 1 au, which could be resolved in a later update (Aibéo, Lima & Sauty 2007). In the deeper solar minimum during FLS3, the polar $\tilde{M}_\mathrm{A}$ is on average slightly greater than the polar $\tilde{M}_\mathrm{A}$ measured during FLS1.

Our estimates of the critical radii r_A, r_S, and r_β assume a constant radial bulk speed of the solar wind between the location of measurement and the respective critical radius. In the inner heliosphere, this assumption can be violated, especially regarding the slow solar wind (Schwenn et al. 1981). Therefore, our calculations only provide lower estimates for the location of these critical radii. The location of the Alfvén radius depends on the magnetic-field geometry near the Sun, which deviates from our simplifying assumption of a Parker profile (Finley & Matt 2017). A dipolar solar braking model constrained by *Ulysses* data estimates that $r_\mathrm{A} \approx 16\,\mathrm{R}_\odot$, independent of heliolatitude (Li 1999). This value is consistent with our largest estimate in regions outside equatorial heliolatitudes. We find a larger variation between this model estimate and ours though. Our findings are in agreement with earlier estimates based on *Helios* measurements in the ecliptic plane, which suggest that $r_\mathrm{A} \approx 12. \ldots 17\,\mathrm{R}_\odot$ (Pizzo et al. 1983; Marsch & Richter 1984). Previous scalings based on a hydrodynamic model also estimate the values of r_A and r_S (Exarhos & Moussas 2000). During solar-minimum conditions, these models suggest that $r_\mathrm{A} \approx 14$ and $r_\mathrm{S} \approx 1.5\,\mathrm{R}_\odot$ at polar heliolatitudes, and that $r_\mathrm{A} \approx 17$ and $r_\mathrm{S} \approx 2\,\mathrm{R}_\odot$ in equatorial regions (for an extension of this model, see also Katsikas, Exarhos & Moussas 2010). While our estimates for r_A are largely consistent with this hydrodynamic model within the observed variability, our estimates of r_S are smaller by a factor of approximately four to five. The reason for this discrepancy in our model is based on the complication that the condition $U_r = c_\mathrm{S}$ is often fulfilled in a region where significant solar-wind acceleration is still ongoing. Since typically $r_\mathrm{S} < r_\mathrm{A}$, our estimate of r_S suffers more strongly from the violation of our assumption that $\partial U_r/\partial r = 0$ than our estimate of r_A. In addition, the extrapolation of the T-profile according to equation (43) from $r = 0.3$ au to distances of a few $R_\odot$ is highly problematic. These shortcomings can be overcome in the future by using (i) a more realistic acceleration profile near the Sun and (ii) a more realistic T-profile near the Sun based on, for example, measurements from *Parker Solar Probe*. Based on OMNI data and their hydrodynamic model, Exarhos & Moussas (2000) predict a dependence of r_A on the solar cycle, which our measurements clearly confirm (see also Kasper & Klein 2019). However, we cannot confirm two predictions made by this model: (i) a more spherical shape of both critical surfaces during solar maximum and (ii) a small variation of r_S with solar cycle. Our estimated positions of r_A and r_β are largely consistent with predictions from a magnetohydrodynamics model of the solar wind over polar regions (Chhiber et al. 2019). We note, however, that our finding of a larger value of $r_\beta \sim 1$ au in the ecliptic plane is more consistent with the observation that, on average, $\beta \sim 1$ at the first Lagrange point (Wilson III et al. 2018). Under the deep solar-minimum conditions during FLS3, we find that, over the poles, the positions of r_A, r_S, and r_β are on average slightly closer to the Sun than during FLS1.

Our calculation neglects any super-radial expansion effects due to expanding flux tubes in the solar wind. These effects can be significant at very small distances from the Sun. Above a few solar radii, however, the super-radial expansion of the coronal magnetic field is expected to be small (Woo & Habbal 1997), although this expectation has been discussed controversially (Neugebauer 1999). If important, the super-radial expansion would especially affect our calculations of r_A and r_S. Nevertheless, all higher-order multipoles of the coronal magnetic field eventually (probably beyond a few solar radii) drop faster than the dipole moment, so that super-radial expansion then becomes negligible (Sandbaek, Leer & Hansteen 1994; Wang et al. 1997).

5 CONCLUSIONS

We use proton and magnetic-field data from the *Ulysses* mission to study the dependence of mass, momentum, energy, and angular-momentum fluxes on heliolatitude. Based on the multifluid framework and assuming an isotropic electron–proton plasma, we derive laws for the radial conservation of these fluxes. These conservation laws allow us to separate the radial dependence from the heliolatitudinal dependence in the *Ulysses* measurements. A major caveat of this method lies in the neglect of the natural spatio-temporal variations in the solar-wind plasma and magnetic field which occur over a wide range of scales (Verscharen, Klein & Maruca 2019). Therefore, our analysis only applies to the average large-scale behaviour of the solar wind. Moreover, we neglect effects due to temporal and heliolongitudinal changes in the source regions of the solar wind. The variability of the flux parameters shown in our analysis, especially during solar maximum, give us an estimate for the natural variability of the solar wind on time-scales greater than our averaging time of 30 h.

Although the *Ulysses* data set is unprecedented in its heliolatitudinal coverage of the solar wind, we expect major advances regarding the topics addressed in this work from the ongoing measurements from *Parker Solar Probe* and *Solar Orbiter*. *Parker Solar Probe* will explore the very inner regions of the heliosphere. Our analysis suggests that it will cross the distance r_A during the later stages of its orbit, while it is unlikely to cross the distance r_S. *Solar Orbiter* will leave the plane of the ecliptic during its extended mission phase and measure the solar wind at heliolatitudes up to $\pm 33^\circ$. Considering that the axial tilt of the Sun's magnetic-field dipole axis is $\lesssim 10^\circ$ during solar minimum (Norton, Raouafi & Petrie 2008), *Solar Orbiter* will cover an even larger range of heliomagnetic latitudes during that phase of the mission.[2] These measurements will therefore

[2]During the early phase of the *Ulysses* mission, a tilt between the Sun's magnetic-field dipole axis and its rotational axis of about 30° has been reported (Bame et al. 1993; Hoeksema 1995).

allow us to study the heliolatitudinal dependence of the relevant solar-wind parameters in a similar way to this study. In addition, both *Parker Solar Probe* and *Solar Orbiter* also provide us with high-resolution measurements of the electron distribution function. Although the electron contributions to the mass, momentum, and angular-momentum fluxes are negligible, their contribution to the energy flux is significant in the form of heat flux (Ogilvie, Scudder & Sugiura 1971; Hollweg 1974; Feldman et al. 1975). It will be worthwhile to include this effect in future studies of this kind. These new observations will help us to further constrain solar-wind models and drive forward our understanding of the acceleration of the solar wind.

Lastly, we emphasize that our observations support the general picture that the solar wind is much more variable during times of solar maximum than during times of solar minimum. This increased variability is likely to be caused by transient events such as interplanetary coronal mass ejections (ICMEs). In our analysis, we include such events in order to reflect the range and pattern of the overall variability on the investigated time-scales. However, it would be worthwhile in a future study to separate our data set into time intervals with and without ICMEs according to existing ICME catalogues for the *Ulysses* data set (e.g. Ebert et al. 2009; Du, Zuo & Zhang 2010; Richardson 2014). This approach would facilitate a detailed study of the contribution of transient events to the variability of mass, momentum, energy, and angular-momentum fluxes. We note, however, that some of our model assumptions, such as the azimuthal symmetry, non-polar field and flow components, and radial scalings must be treated with caution in transient events. In addition, we also find a significant variation in some of the analysed quantities between the solar minima recorded during FLS1 and FLS3. It is of interest to study these conditions more closely. This should especially include a closer inspection of the question to what degree the observed variations are real and to what degree they result from breakdowns in our assumptions.

ACKNOWLEDGEMENTS

DV is supported by the Science and Technology Facilities Council (STFC) Ernest Rutherford Fellowship ST/P003826/1 and STFC Consolidated Grant ST/S000240/1. SDB acknowledges the support of the Leverhulme Trust Visiting Professorship programme. The authors acknowledge insightful discussions within the International Team 'Exploring The Solar Wind In Regions Closer Than Ever Observed Before' at the International Space Science Institute (ISSI) in Bern led by Louise Harra. We acknowledge the National Space Science Data Center for the provision of the *Ulysses* data.

DATA AVAILABILITY

All used data are freely available online at NASA's National Space Science Data Center under https://nssdc.gsfc.nasa.gov.

REFERENCES

Aibéo A., Lima J. J. G., Sauty C., 2007, A&A, 461, 685
Alexander P., de La Torre A., 1995, Sol. Phys., 157, 367
Balogh A., 1994, Phil. Trans. R. Soc. A, 349, 227
Balogh A., Beek T. J., Forsyth R. J., Hedgecock P. C., Marquedant R. J., Smith E. J., Southwood D. J., Tsurutani B. T., 1992, A&AS, 92, 221
Bame S. J., Goldstein B. E., Gosling J. T., Harvey J. W., McComas D. J., Neugebauer M., Phillips J. L., 1993, Geophys. Res. Lett., 20, 2323
Bame S. J., McComas D. J., Barraclough B. L., Phillips J. L., Sofaly K. J., Chavez J. C., Goldstein B. E., Sakurai R. K., 1992, A&AS, 92, 237
Barnes A., Gazis P. R., Phillips J. L., 1995, Geophys. Res. Lett., 22, 3309
Brandt J. C., Heise J., 1970, ApJ, 159, 1057
Bruno R., Carbone V., 2013, Liv. Rev. Sol. Phys., 10, 2
Bruno R., Dobrowolny M., 1986, Ann. Geophys., 4, 17
Bruno R., Villante U., Bavassano B., Schwenn R., Mariani F., 1986, Sol. Phys., 104, 431
Chhiber R., Usmanov A. V., Matthaeus W. H., Goldstein M. L., 2019, ApJS, 241, 11
Cranmer S. R., Gibson S. E., Riley P., 2017, Space Sci. Rev., 212, 1345
D'Amicis R., Bruno R., Pallocchia G., Bavassano B., Telloni D., Carbone V., Balogh A., 2010, ApJ, 717, 474
Du D., Zuo P. B., Zhang X. X., 2010, Sol. Phys., 262, 171
Ebert R. W., McComas D. J., Elliott H. A., Forsyth R. J., Gosling J. T., 2009, J. Geophys. Res., 114, A01109
Egidi A., Pizzella G., Signorini C., 1969, J. Geophys. Res., 74, 2807
Exarhos G., Moussas X., 2000, A&A, 356, 315
Feldman W. C., Asbridge J. R., Bame S. J., Gosling J. T., 1978, J. Geophys. Res., 83, 2177
Feldman W. C., Asbridge J. R., Bame S. J., Montgomery M. D., Gary S. P., 1975, J. Geophys. Res., 80, 4181
Finley A. J. et al., 2020, ApJ, 902, L4
Finley A. J., Hewitt A. L., Matt S. P., Owens M., Pinto R. F., Réville V., 2019, ApJ, 885, L30
Finley A. J., Matt S. P., 2017, ApJ, 845, 46
Finley A. J., Matt S. P., See V., 2018, ApJ, 864, 125
Fisk L. A., 1996, J. Geophys. Res., 101, 15547
Forsyth R. J., Balogh A., Horbury T. S., Erdoes G., Smith E. J., Burton M. E., 1996b, A&A, 316, 287
Forsyth R. J., Balogh A., Smith E. J., Erdös G., McComas D. J., 1996a, J. Geophys. Res., 101, 395
Fox N. J. et al., 2016, Space Sci. Rev., 204, 7
Goldstein B. E. et al., 1996, A&A, 316, 296
Hellinger P., Matteini L., Štverák Š., Trávníček P. M., Marsch E., 2011, J. Geophys. Res., 116, A09105
Hoeksema J. T., 1995, Space Sci. Rev., 72, 137
Hollweg J. V., 1974, J. Geophys. Res., 79, 3845
Holzer T. E., Leer E., 1980, J. Geophys. Res., 85, 4665
Hundhausen A. J., 1970, Rev. Geophys. Space Phys., 8, 729
Hundhausen A. J., Bame S. J., Asbridge J. R., Sydoriak S. J., 1970, J. Geophys. Res., 75, 4643
Jokipii J. R., 2013, Space Sci. Rev., 176, 115
Kasper J. C. et al., 2019, Nature, 576, 228
Kasper J. C., Klein K. G., 2019, ApJL, 877, L35
Katsikas V., Exarhos G., Moussas X., 2010, Adv. Space Res., 46, 382
Lazarus A. J., Goldstein B. E., 1971, ApJ, 168, 571
Le Chat G., Issautier K., Meyer-Vernet N., 2012, Sol. Phys., 279, 197
Li J., 1999, MNRAS, 302, 203
Marsch E., Richter A. K., 1984, J. Geophys. Res., 89, 5386
Marsch E., Rosenbauer H., Schwenn R., Muehlhaeuser K. H., Neubauer F. M., 1982a, J. Geophys. Res., 87, 35
Marsch E., Schwenn R., Rosenbauer H., Muehlhaeuser K. H., Pilipp W., Neubauer F. M., 1982b, J. Geophys. Res., 87, 52
Marsden R. G., 2001, Ap&SS, 277, 337
Matthaeus W. H., Goldstein M. L., 1982, J. Geophys. Res., 87, 6011
McComas D. J. et al., 1998a, Geophys. Res. Lett., 25, 1
McComas D. J. et al., 2000, J. Geophys. Res., 105, 10419
McComas D. J., Angold N., Elliott H. A., Livadiotis G., Schwadron N. A., Skoug R. M., Smith C. W., 2013, ApJ, 779, 2
McComas D. J., Ebert R. W., Elliott H. A., Goldstein B. E., Gosling J. T., Schwadron N. A., Skoug R. M., 2008, Geophys. Res. Lett., 35, L18103
McComas D. J., Elliott H. A., Gosling J. T., Reisenfeld D. B., Skoug R. M., Goldstein B. E., Neugebauer M., Balogh A., 2002, Geophys. Res. Lett., 29, 1290
McComas D. J., Riley P., Gosling J. T., Balogh A., Forsyth R., 1998b, J. Geophys. Res., 103, 1955
Mestel L., 1968, MNRAS, 138, 359

Müller D. et al., 2020, A&A, 642, A1
Munro R. H., Jackson B. V., 1977, ApJ, 213, 874
Neugebauer M., 1999, Rev. Geophys., 37, 107
Norton A. A., Raouafi N. E., Petrie G. J. D., 2008, ApJ, 682, 1306
Ogilvie K. W., Scudder J. D., Sugiura M., 1971, J. Geophys. Res., 76, 8165
Parker E. N., 1958, ApJ, 128, 664
Phillips J. L. et al., 1995, Geophys. Res. Lett., 22, 3301
Pizzo V., Schwenn R., Marsch E., Rosenbauer H., Muehlhaeuser K. H., Neubauer F. M., 1983, ApJ, 271, 335
Réville V., Brun A. S., 2017, ApJ, 850, 45
Richardson I. G., 2014, Sol. Phys., 289, 3843
Sandbaek O., Leer E., Hansteen V. H., 1994, ApJ, 436, 390
Sauty C., Lima J. J. G., Iro N., Tsinganos K., 2005, A&A, 432, 687
Schwenn R., Mohlhauser K. H., Marsch E., Rosenbauer H., 1981, in Solar Wind Four, Max Planck Institute for Aeronomy, Katlenburg-Lindau, Germany. p. 126
Siscoe G. L., Goldstein B., Lazarus A. J., 1969, J. Geophys. Res., 74, 1759
Tu C. Y., Marsch E., 1995, Space Sci. Rev., 73, 1
Verscharen D. et al., 2021, A&A, accepted, preprint (arXiv:2106.01780)
Verscharen D., Chandran B. D. G., Bourouaine S., Hollweg J. V., 2015, ApJ, 806, 157
Verscharen D., Klein K. G., Maruca B. A., 2019, Liv. Rev. Sol. Phys., 16, 5
Wang Y. M., 2010, ApJ, 715, L121
Wang Y. M., Sheeley N. R. J., Phillips J. L., Goldstein B. E., 1997, ApJ, 488, L51
Weber E. J., Davis Leverett J., 1967, ApJ, 148, 217
Wenzel K. P., Marsden R. G., Page D. E., Smith E. J., 1992, A&AS, 92, 207
Wilson III L. B. et al., 2018, ApJS, 236, 41
Woo R., Habbal S. R., 1997, Geophys. Res. Lett., 24, 1159

This paper has been typeset from a TEX/LATEX file prepared by the author.